



## Pore structure characterization of North American shale gas reservoirs using USANS/SANS, gas adsorption, and mercury intrusion

C.R. Clarkson<sup>a,\*</sup>, N. Solano<sup>a</sup>, R.M. Bustin<sup>b</sup>, A.M.M. Bustin<sup>b</sup>, G.R.L. Chalmers<sup>b</sup>, L. He<sup>c</sup>, Y.B. Melnichenko<sup>c</sup>, A.P. Radliński<sup>d,e</sup>, T.P. Blach<sup>d</sup>

<sup>a</sup> Department of Geoscience, University of Calgary, 2500 University Drive NW, Calgary, Alberta, Canada T2N 1N4

<sup>b</sup> Department of Earth and Ocean Sciences, 6339 Stores Rd., Vancouver, British Columbia, Canada V6Z 1Z4

<sup>c</sup> Neutron Scattering Sciences Division, Oak Ridge National Laboratory, Oak Ridge, TN 37831, USA

<sup>d</sup> Griffith University, Queensland Micro and Nanotechnology Centre, Kessels Rd., Nathan, Brisbane, Queensland 4111, Australia

<sup>e</sup> Indiana Geological Survey, Indiana University, 611 North Walnut Grove, Bloomington, IN, USA

### HIGHLIGHTS

- ▶ SANS/USANS is used to characterize pore structure of shale gas reservoirs.
- ▶ SANS/USANS results are compared to gas adsorption and mercury intrusion.
- ▶ There are substantial differences in surface areas and pore size distributions between samples.
- ▶ Pore size distributions from gas adsorption and SANS/USANS are in reasonable agreement.
- ▶ Accessible porosity estimates were obtained for a Barnett shale sample.

### ARTICLE INFO

#### Article history:

Received 30 March 2012

Received in revised form 28 June 2012

Accepted 29 June 2012

Available online 13 July 2012

#### Keywords:

Shale gas

Pore structure

Small-angle neutron scattering

Gas adsorption

Mercury intrusion

### ABSTRACT

Small-angle and ultra-small-angle neutron scattering (SANS and USANS), low-pressure adsorption (N<sub>2</sub> and CO<sub>2</sub>), and high-pressure mercury intrusion measurements were performed on a suite of North American shale reservoir samples providing the first ever comparison of all these techniques for characterizing the complex pore structure of shales. The techniques were used to gain insight into the nature of the pore structure including pore geometry, pore size distribution and accessible versus inaccessible porosity. Reservoir samples for analysis were taken from currently-active shale gas plays including the Barnett, Marcellus, Haynesville, Eagle Ford, Woodford, Muskwa, and Duvernay shales.

Low-pressure adsorption revealed strong differences in BET surface area and pore volumes for the sample suite, consistent with variability in composition of the samples. The combination of CO<sub>2</sub> and N<sub>2</sub> adsorption data allowed pore size distributions to be created for micro–meso–macroporosity up to a limit of ~1000 Å. Pore size distributions are either uni- or multi-modal. The adsorption-derived pore size distributions for some samples are inconsistent with mercury intrusion data, likely owing to a combination of grain compression during high-pressure intrusion, and the fact that mercury intrusion yields information about pore throat rather than pore body distributions.

SANS/USANS scattering data indicate a fractal geometry (power-law scattering) for a wide range of pore sizes and provide evidence that nanometer-scale spatial ordering occurs in lower mesopore–micropore range for some samples, which may be associated with inter-layer spacing in clay minerals. SANS/USANS pore radius distributions were converted to pore volume distributions for direct comparison with adsorption data. For the overlap region between the two methods, the agreement is quite good. Accessible porosity in the pore size (radius) range 5 nm–10 μm was determined for a Barnett shale sample using the contrast matching method with pressurized deuterated methane fluid. The results demonstrate that accessible porosity is pore-size dependent.

© 2012 Elsevier Ltd. All rights reserved.

## 1. Introduction

The matrix pore structure of shale gas reservoirs is difficult to characterize because a significant portion of total matrix porosity

\* Corresponding author.

E-mail address: [clarkso@ucalgary.ca](mailto:clarkso@ucalgary.ca) (C.R. Clarkson).

may be distributed in ultra-fine (nano) pores associated with organic matter and clays. Further, shales commonly exhibit a wide pore size distribution necessitating the use of multiple techniques to investigate the full pore size range. A combination of fluid invasion and radiation methods have historically been used for the characterization of shale samples [1]. Knowledge of pore size distribution is critical for understanding both fluid flow mechanisms and storage [2].

The fluid invasion methods that have typically been used for pore structure characterization of shale include a combination of high-pressure mercury intrusion (MICP), which requires immense injection pressures to access the finest porosity, and low-pressure adsorption (LPA) using N<sub>2</sub> and CO<sub>2</sub> as adsorbates. Mercury intrusion is useful for characterizing meso- (pore diameters between 2 and 50 nm) and macro-porosity (pore diameters > 50 nm), but some pore structure distortion may occur at the lower pore size limit (~3 nm) due to compressibility effects [1]. In addition, the technique requires drying of the samples, which could alter porosity and fabric of shales with high clay content [1]. Low-pressure adsorption of CO<sub>2</sub> is useful for characterizing microporosity (pore diameters < 2 nm), while LPA of nitrogen is useful for characterizing meso- and macroporosity. Unfortunately, LPA has an upper pore diameter limit of ~300 nm [2]. Further, this technique requires drying and evacuation of the samples to remove volatiles prior to analysis. There exists an “overlap” pore size region for which MICP and LPA can be compared. Comparisons of MICP and LPA have historically been performed for coals [3–5] and more recently gas shales [1,6–9].

Small-angle neutron scattering (SANS), combined with ultra-small-angle neutron scattering (USANS) allows for a wide pore size distribution to be investigated, as demonstrated recently for coals [10–14] and siltstones [15]. Moreover, analysis may be performed at elevated temperature and pressure, unlike LPA, and is non-destructive, unlike MICP. Combined SANS/USANS provides an estimate of total porosity and pore size distribution (PSD), which can be compared with accessible porosity and PSD provided by LPA and MICP. The accessible porosity (and PSD) for fluid invasion techniques is a function of adsorbate molecular size, temperature and pressure of analysis. Accessible porosity can also be determined from SANS/USANS alone, as demonstrated recently by Melnichenko et al. [16]. Further, pore structure information can be more confidently extracted from SANS/USANS, because the interpretation is independent of fluid/surface interaction or percolation effects. SANS/USANS is therefore a very powerful, albeit non-routine, analysis technique that can be employed to independently verify and supplement results obtained using more routine methods such as MICP and LPA.

In this work, we investigate the pore structure of several North American shale gas plays using SANS/USANS, low-pressure adsorption and mercury intrusion techniques. Pore size distributions are compared for the various methods. Although the controls of mineralogy on the pore structure for all samples analyzed are inferred, a more detailed study of these effects will be discussed in a future article.

## 2. Experimental methods

Samples from seven North American shale plays were cut from fresh cores for analysis in this study. Two samples were taken from the Muskwa and Woodford shale plays, and one sample each from the Duvernay, Haynesville, Marcellus, Eagle Ford and Barnett Shale gas plays. In addition, a montmorillonite-rich sample from the Late Cretaceous Milk River Formation in central Alberta, Canada was studied. Table 1 lists the shale samples analyzed, including the for-

**Table 1**  
Shale sample properties.

| Shale reservoir | Sample name | Age             | TOC (wt.%) | R <sub>o</sub> <sup>a</sup> (%) |
|-----------------|-------------|-----------------|------------|---------------------------------|
| Milk River      | MONT2       | Late Cretaceous | 1.28       | 0.7                             |
| Duvernay        | DUVERNAY    | Late Devonian   | 3.84       | 1.4                             |
| Eagle Ford      | EAGLEFORD   | Late Cretaceous | 2.63       | 1.65                            |
| Muskwa          | MUSKWA1     | Late Devonian   | 2.95       | 1.6                             |
| Muskwa          | MUSKWA2     | Late Devonian   | NA         | NA                              |
| Woodford        | WOODFORD1   | Late Devonian   | 2.77       | 1.4                             |
| Woodford        | WOODFORD2   | Late Devonian   | 1.55       | 1.4                             |
| Barnett         | BARNETT     | Mississippian   | 4.11       | 1.45                            |
| Haynesville     | HAYNESVILLE | Late Jurassic   | 3.94       | 2.0                             |
| Marcellus       | MARCELLUS   | Middle Devonian | 1.57       | 1.2                             |

<sup>a</sup> Values are approximate.

mation from which they were sampled, their age, total organic carbon content (TOC), and thermal maturity.

The samples for all analyses were prepared by cutting 17 mm diameter cores in air parallel to bedding from preserved core. For SANS and USANS the cores were cut to about 2 mm thick with a wafer saw. The samples were then polished to their final thickness using a precision machined fixture such that the final wafer thickness was 1.0 mm (±5%) thick. For SANS/USANS analysis, the discs were ground further to 14 mm to fit into the high-pressure cell (described below).

SANS experiments were performed on the General Purpose SANS instrument at the Oak Ridge National Laboratory [17] using a neutron wavelength of  $\lambda = 12 \text{ \AA}$  and  $\lambda = 4.8 \text{ \AA}$  ( $\Delta\lambda/\lambda \sim 0.13$ ). Sample-detector distances were chosen to cover an overall range of scattering vectors ( $Q$ )  $0.0016 < Q < 0.7 \text{ \AA}^{-1}$ , where  $Q = 4\pi\lambda^{-1}\sin\theta$ , in which  $2\theta$  is the scattering angle. Data were corrected for instrumental background as well as detector efficiency and put on absolute scale [cross section  $I(Q)$  in units of  $\text{cm}^{-1}$ ] by means of pre-calibrated secondary standards. USANS experiments were performed at NIST, using the BT5 perfect crystal SANS instrument ( $\lambda = 2.4 \text{ \AA}$ ,  $Q$ -range  $5 \times 10^{-5} < Q < 0.00266 \text{ \AA}^{-1}$  (Barker et al. [18]). The neutron beam size used was about  $3 \text{ cm}^2$  in area and the total acquisition time was of the order of 60 min for SANS (total acquisition time at three sample-detector distances) and approximately 7 h for USANS.

Use of these instruments allowed a broad range of pore sizes to be probed by neutrons, from approximately 100,000  $\text{Å}$  to 5  $\text{Å}$ . Characteristic pore size ( $r$ ) may be estimated based on the Bragg law  $\lambda = 2D\sin\theta$ , where for disordered systems  $D$  is the characteristic length scale of the structural inhomogeneities (e.g. linear size of pores embedded in a rock matrix, which provide most scattering intensity measured at the scattering angle  $\theta$ ). This law provides an approximate relationship between the scattering vector  $Q$  and  $r$ :  $2r \approx 2\pi/Q$ , where  $r$  is pore radius. Detailed simulations show that for polydisperse porous media a more appropriate relationship is  $r \approx 2.5/Q$  (Radlinski et al. [19]), which was used in this work to relate  $Q$ -values with  $r$ .

Prior to the experiments, the samples were dried under vacuum at 60 °C for at least 24 h; the observed weight change attributable to the humidity reduction did not exceed 2.1% on any sample.

We note that some microstructural changes to the samples may have occurred due to de-watering during some stages of sample preparation. As noted by Bustin et al. [1], the impact of drying on pore structure is shale-specific.

The majority of the experiments were run at ambient conditions, with additional measurements collected at several combinations of pressure and/or temperature for the Barnett sample (Table 2). For the scans run at ambient conditions, the samples were confined in standard demountable cells with titanium body and quartz windows. A high-pressure cell designed at ORNL was used to hold the samples for the non-ambient conditions scans, and deuterated

**Table 2**  
SANS/USANS run conditions.

| Shale reservoir | Sample name | Analysis Method    | P (bar) | T (°C)  |
|-----------------|-------------|--------------------|---------|---------|
| Barnett         | BARNETT     | USANS              | Ambient | 80      |
| Barnett         | BARNETT     | USANS              | 207.3   | 80      |
| Barnett         | BARNETT     | USANS              | 348.8   | 80      |
| Barnett         | BARNETT     | USANS              | 416.4   | 80      |
| Barnett         | BARNETT     | USANS              | 485.7   | 80      |
| Barnett         | BARNETT     | USANS              | 551.7   | 80      |
| Barnett         | BARNETT     | USANS <sup>a</sup> | 345.0   | 80      |
| Barnett         | BARNETT     | USANS <sup>a</sup> | 486.1   | 80      |
| Barnett         | BARNETT     | USANS <sup>a</sup> | 416.4   | 80      |
| Barnett         | BARNETT     | USANS <sup>a</sup> | 348.8   | 80      |
| Barnett         | BARNETT     | USANS <sup>a</sup> | 276.1   | 80      |
| Barnett         | BARNETT     | SANS               | Ambient | 80      |
| Barnett         | BARNETT     | SANS               | 206.8   | 80      |
| Barnett         | BARNETT     | SANS               | 551.6   | 80      |
| Milk River      | MONT2       | USANS              | Ambient | Ambient |
| Milk River      | MONT2       | SANS               | Ambient | Ambient |
| Duvernay        | DUVERNAY    | USANS              | Ambient | Ambient |
| Duvernay        | DUVERNAY    | SANS               | Ambient | Ambient |
| Eagle Ford      | EAGLEFORD   | USANS              | Ambient | Ambient |
| Eagle Ford      | EAGLEFORD   | SANS               | Ambient | Ambient |
| Haynesville     | HAYNESVILLE | USANS              | Ambient | Ambient |
| Haynesville     | HAYNESVILLE | SANS               | Ambient | Ambient |
| Marcellus       | MARCELLUS   | USANS              | Ambient | Ambient |
| Marcellus       | MARCELLUS   | SANS               | Ambient | Ambient |

<sup>a</sup> Pressure scan runs.

methane (CD<sub>4</sub>) was used as the injection fluid. SANS measurements with this cell, which has been used extensively for scattering experiments performed on coal [e.g. 11,12] as well as engineered porous media [20], enabled monitoring of pore structure and CD<sub>4</sub> (Air Liquide, 99% purity) storage under pressure. A custom-built pressure intensifier was used to increase the pressure stepwise inside the cell, and its value was monitored using a precision pressure transducer. A stabilization time of 10 min followed the fluid injection at each pressure step to allow for equilibrium to be achieved between CD<sub>4</sub> and the shale sample.

Multiple pressure scans using the high-pressure cell were also used to calculate the zero average contrast pressure ( $P_{ZAC}$ ) for the Barnett sample. The residual scattering at the  $P_{ZAC}$  combined with the procedure described by Melnichenko et al. [16] was used to determine the amount of inaccessible pores in this sample.

Samples prepared for adsorption analysis were first outgassed for a minimum of 4 days in a vacuum oven. N<sub>2</sub> adsorption isotherms were collected at 77 K using a Quantachrome Autosorb

–1 on –60 mesh samples. CO<sub>2</sub> adsorption data (273 K) were also collected on the same apparatus. The N<sub>2</sub> data collected on crushed samples were interpreted using multi-point Brunauer–Emmett–Teller (BET) and Langmuir analysis for surface area and Barrett–Joyner–Halenda (BJH) analysis for pore size distributions – these methods are comprehensively discussed in Gregg and Sing [21]. CO<sub>2</sub> adsorption data were interpreted using the BET and Langmuir models, as well as the Dubinin–Astakhov (D–A) and Dubinin–Radushkevich (D–R) models.

Mercury intrusion analysis was performed on vacuum dried samples using a Micrometrics Autopore IV at pressures up to 60,000 psia.

Additional data collected on shale sub-samples included X-ray Diffraction (XRD). The samples were milled to ultrafine particle size and random grain mounts prepared and analyzed. XRD was performed with a normal focus Cobalt X-ray tube used in a Siemens Diffractometer D8 at 40 mA and 40 kV and mineralogy was quantified by Rietveld analyses [22] using the software Topas.

### 3. Results

#### 3.1. XRD analysis

Mineral percentages for the Barnett, Haynesville, Montmorillonite-rich (“Mont 2”), Marcellus, Duvernay, Eagle Ford, one Woodford and two Muskwa samples (“Muskwa 1” and “Muskwa 2”) are given in Fig. 1 and demonstrate a wide range in inorganic fraction compositions for this North American shale suite. The dominant minerals are quartz, calcite, muscovite and illite; we note that muscovite and illite are difficult to distinguish with Rietveld analyses [22]. Illite-rich shales have been demonstrated to contain a significant micropore volume (ex. Kuila and Prasad [23]), and hence this differentiation would be important for determining controls on pore structure. The Barnett and Muskwa (1 and 2) samples have the highest quartz content, while the Marcellus sample has the lowest. The Marcellus and Eagle Ford samples have a relatively high calcite content. The montmorillonite-rich sample shows a dominance of smectite-group clays, but also contains kaolinite, albite, muscovite/illite and quartz.

#### 3.2. N<sub>2</sub> and CO<sub>2</sub> adsorption

As discussed by Bustin et al. [1], CO<sub>2</sub> adsorption at 0 °C can be used to investigate micropore volume and N<sub>2</sub> adsorption at –196 °C can be used to investigate pore volume in the larger

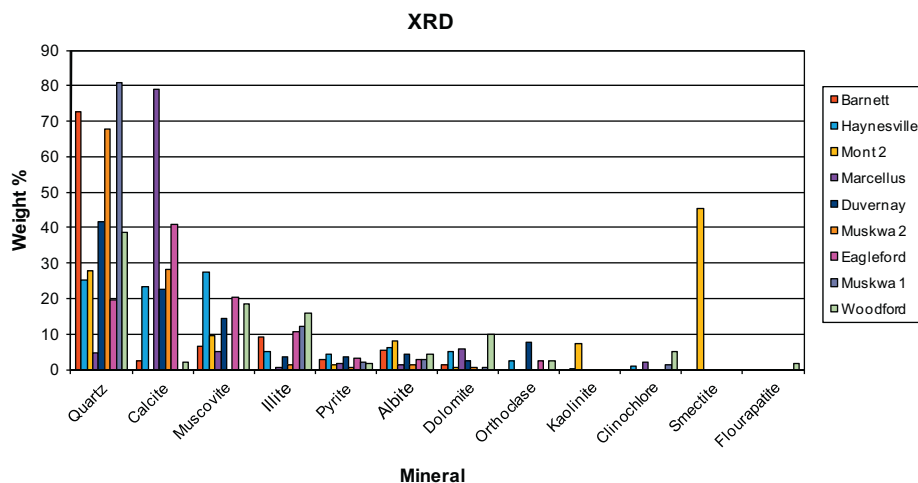


**Fig. 1.** Comparison of mineralogical composition of the shale samples based on XRD analysis.

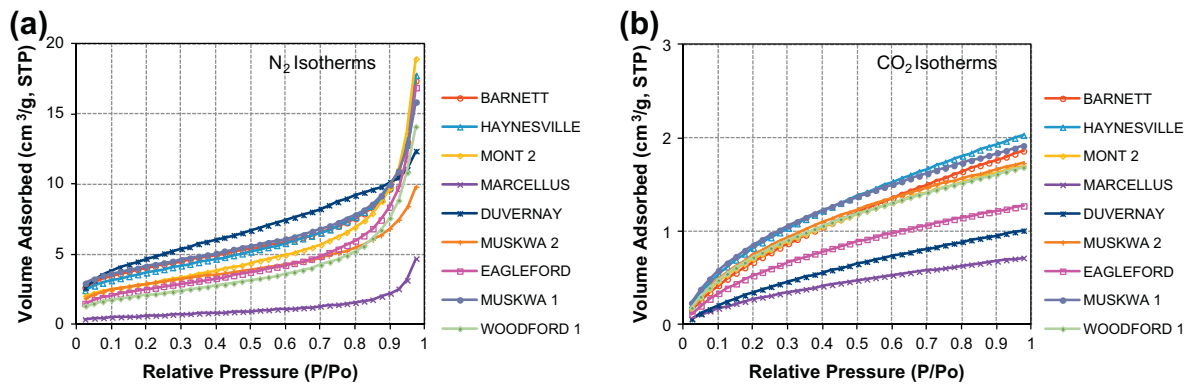


Fig. 2. Nitrogen (a) and carbon dioxide (b) isotherms collected for the shale samples. Note that relative pressure refers to the ratio of vapor pressure of the analysis gas to the saturation vapor pressure of that gas.

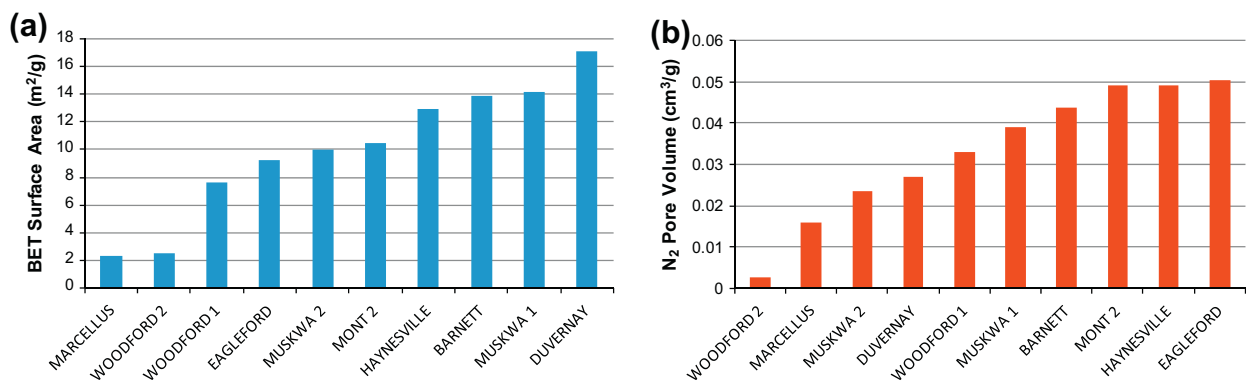


Fig. 3. Nitrogen BET surface areas (a) and pore volume (b) for the shale samples.

micropore to macropore range.  $N_2$  and  $CO_2$  adsorption isotherms (Fig. 2) demonstrate a wide range in adsorption for all samples.

$N_2$  adsorption isotherms (Fig. 2a) are Type II according to the Brunauer, Deming, Deming and Teller classification [24], indicative of multi-layer adsorption, and analyzable using BET Theory [21]. The tests were performed with increasing  $N_2$  pressure only (adsorption branch) and no desorption data was collected to establish whether a hysteresis loop would be obtained. Previous studies [23] indicate that Type IV isotherms (isotherms with hysteresis loop) are common for shale as is the presence of mesoporosity. At relative pressures below 0.9, the Duvernay sample exhibits the highest  $N_2$  adsorption, whereas the Marcellus sample exhibits the least. The Duvernay isotherm is somewhat unusual in that it has the steepest slope up until a relative pressure of 0.9, but does not show as steep of a rise above this pressure. All other samples exhibit similar isotherm shapes. A significant amount of adsorption at low relative pressure ( $<0.05$ ) for all samples (except Marcellus) is indicative of microporosity.

$CO_2$  adsorption isotherms (Fig. 2b) are Type I, indicative of microporous solids. The Marcellus sample again displays the least amount of adsorption, suggesting little microporosity, but the Haynesville sample now exhibits the highest adsorption.

BET surface areas and pore volumes, obtained from  $N_2$  adsorption analysis, similarly exhibit a wide range for the samples (Fig. 3). The Duvernay exhibits the highest surface area ( $17.1 \text{ m}^2/\text{g}$ ) and the Marcellus sample the least ( $2.3 \text{ m}^2/\text{g}$ ), with the average surface area of the samples being  $10.0 \text{ m}^2/\text{g}$ . These values are quite large compared to the siltstone samples analyzed by Clarkson et al. [15], except for the Marcellus and Woodford2 samples. The Haynesville and Eagle Ford samples have the largest pore volumes as determined by BJH theory, while the Woodford2 sample has the smallest.

There is also a substantial variation in micropore volume as determined from  $CO_2$  adsorption analysis (Fig. 4). The Marcellus, Duvernay and Woodford 2 samples have the smallest micropore volumes, while Haynesville, Muskwa 1 and Barnett have the largest.

Plots of cumulative pore volume versus pore size for nitrogen and carbon dioxide (Fig. 5) illustrate the distribution of pore volumes (with respect to pore size) for the samples. From  $N_2$  analysis, which is restricted primarily to pore radii  $>6 \text{ \AA}$  ( $0.6 \text{ nm}$ ), we see that the Duvernay sample has the greatest amount of pore volume in the pore size (radius) range of  $6\text{--}170 \text{ \AA}$  ( $6\text{--}17 \text{ nm}$ ), but all other samples except Muskwa 2, Marcellus and Woodford 2, have greater pore volumes in the  $170\text{--}1000 \text{ \AA}$  ( $17\text{--}100 \text{ nm}$ ) range. The Eagle Ford, Haynesville, Barnett and Mont 2 samples have the largest

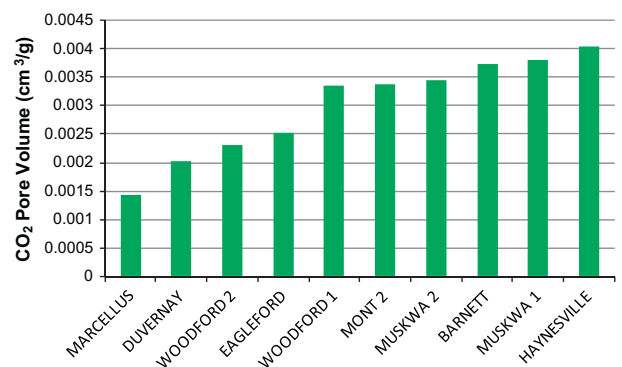


Fig. 4. Micropore volume of shale sample suite as determined by carbon dioxide adsorption.

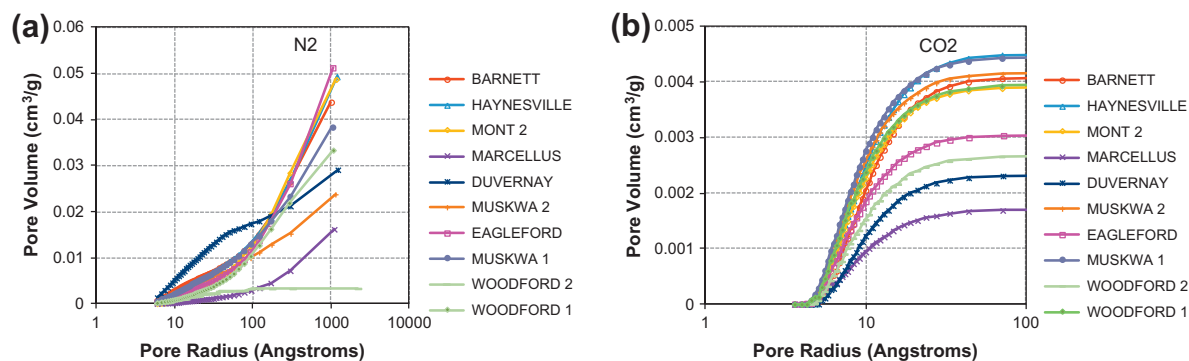


Fig. 5. Cumulative adsorption pore volumes using (a) nitrogen and (b) carbon dioxide.

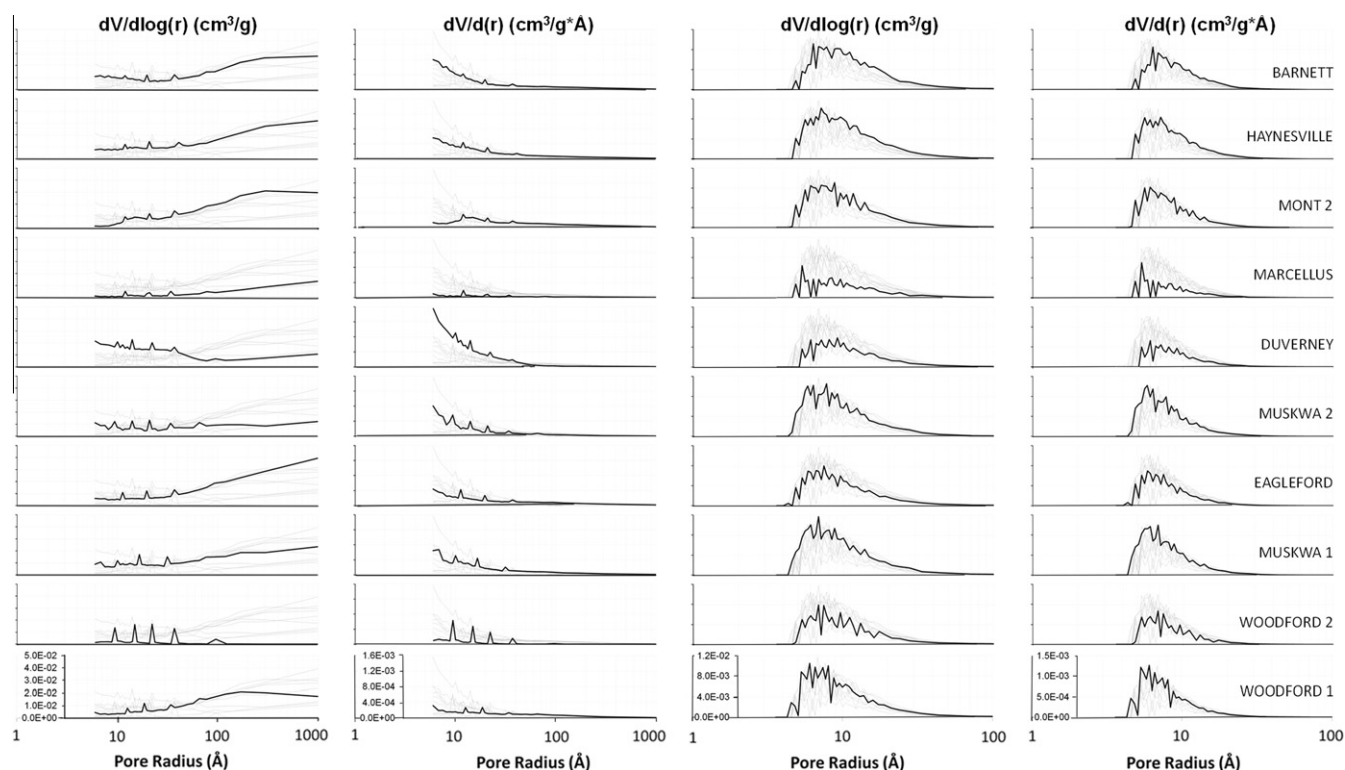


Fig. 6. Pore volume distributions using nitrogen (columns 1 and 2) and carbon dioxide (columns 3 and 4).

pore volumes in this range. CO<sub>2</sub> sorption analysis, which allows slightly finer pore sizes to be investigated, appears to reach a saturation limit at 50 Å (5 nm).

N<sub>2</sub> pore volume distributions (Fig. 6) reveal that the shale pore structure may be unimodal or multi-modal. The  $dV/d\log r$  plots (column 1 of Fig. 6) suggest bimodality for some samples (peaks at  $\sim 6$  Å and  $>100$  Å whereas the  $dV/dr$  plots (column 2) suggest unimodality with a peak around 6 Å. We note that the  $dV/d\log r = \ln 10 \times r dV/dr$ , meaning that the derivative ( $y$ -axis value) is markedly expanded for larger pore sizes. Note that apparent noise in the pore size distributions may be caused by minor temperature fluctuations during the experiments, which are amplified when the derivative is taken.

The N<sub>2</sub>  $dV/d\log r$  plots for the Barnett, two Woodford samples, two Muskwa samples and the Montmorillonite-rich sample (Mont 2) are shown in Fig. 7 to more clearly illustrate end-member N<sub>2</sub> PSD behavior. The Barnett sample appears to be bimodal, with peaks near 10 and 1000 Å. The Mont 2 sample exhibits similar

characteristics – the PSD for this sample looks very similar to the montmorillonite powder examined by Kuila and Prasad [23]. The two Woodford samples exhibit very different PSDs, whereas the two Muskwa samples are similar.

The CO<sub>2</sub>  $dV/d\log r$  and  $dV/dr$  plots (columns 3,4 of Fig. 6) suggest a unimodal PSD in the micropore range ( $<10$  Angstroms), with the peak corresponding reasonably well with the first peak of the N<sub>2</sub> distributions. The continuity of the CO<sub>2</sub> and N<sub>2</sub> pore volume distributions is illustrated more clearly in Fig. 8 for the Barnett and Mont 2 samples. The CO<sub>2</sub> and N<sub>2</sub> curves end and start at 10 Å, respectively, and show a near seamless transition. All the other samples demonstrate a similarly smooth transition, with the exception of the Duvernay sample – we are uncertain of the cause of this discrepancy, but it may be related to residual solid bitumen in the samples. The Duvernay sample is the only one in the suite that has a measurable oil saturation. For this sample, the N<sub>2</sub> peak at 10 Å is much greater than CO<sub>2</sub>.

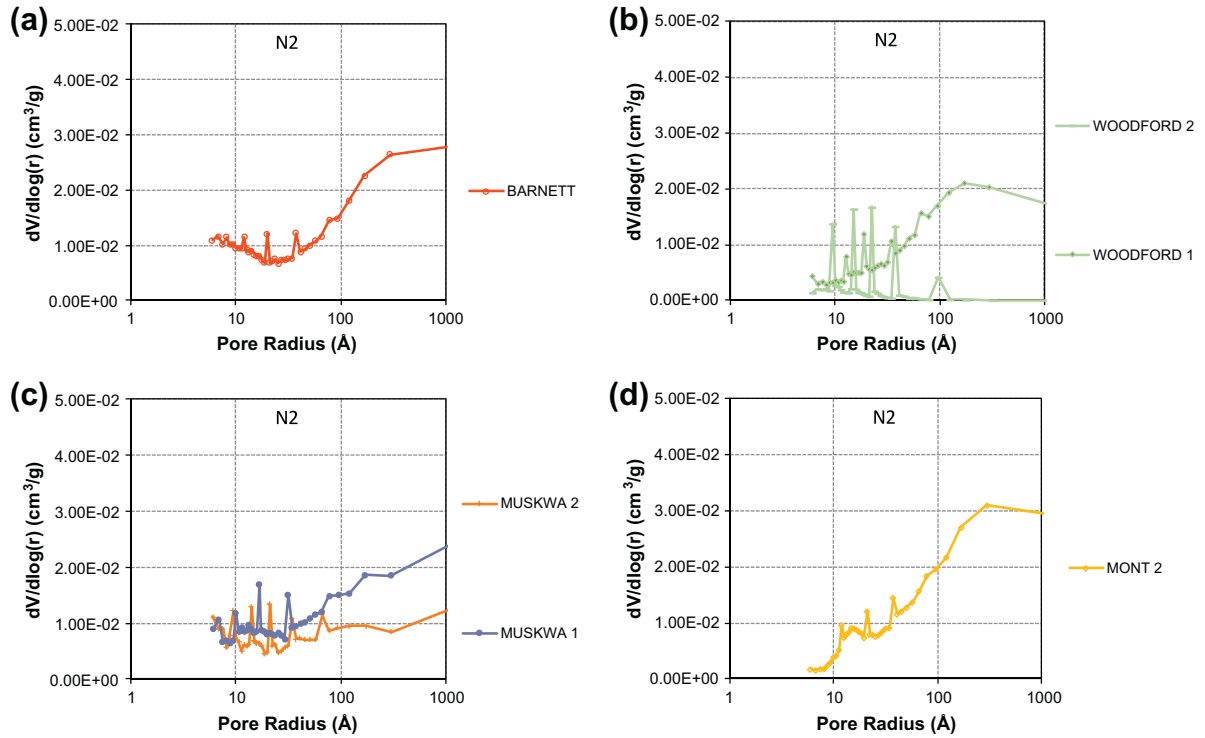


Fig. 7. N<sub>2</sub> dV/dlogr plots for Barnett (a), Woodford (b), Muskwa (c) and Mont 2 (d) samples.

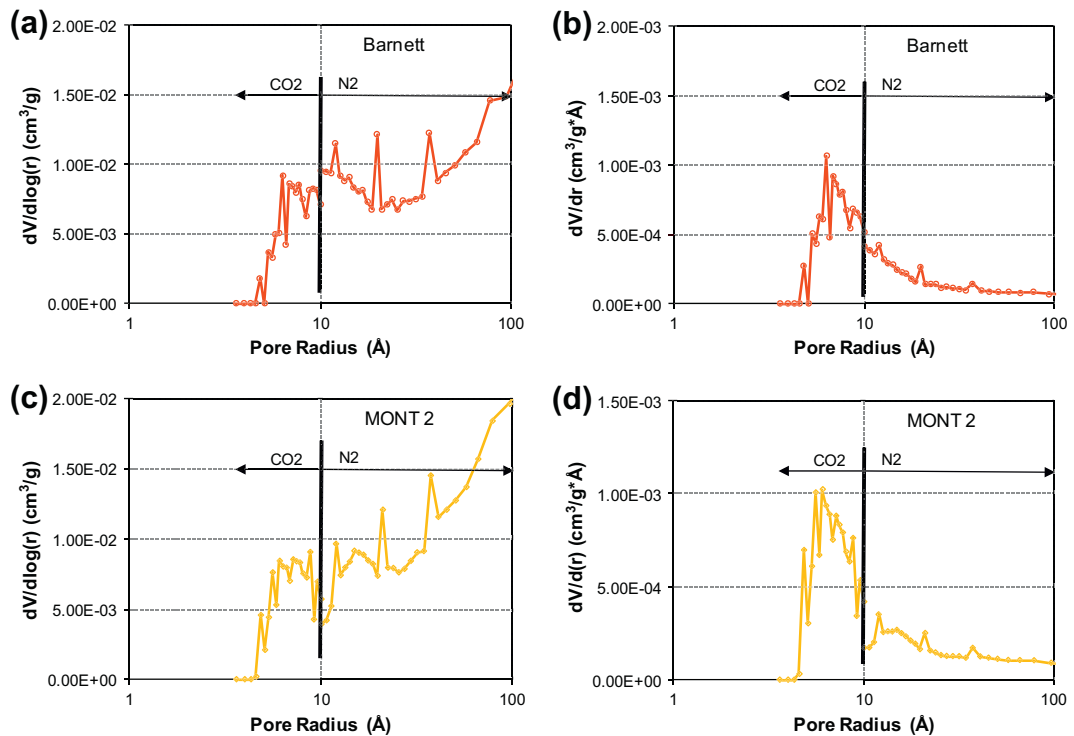


Fig. 8. Combined nitrogen and carbon dioxide pore volume distributions for Barnett sample (a and b) and Mont 2 sample (c and d). Note that the y-axis in a and c is  $dv/dlogr$  and  $dv/dr$  in b and d. Arrows indicate range of pore sizes covered by N<sub>2</sub> and CO<sub>2</sub> adsorption.

In this study, N<sub>2</sub> pore volume and pore volume distributions appear to suggest that N<sub>2</sub> penetrates smaller pores (pore radii < 10 Å, or 1 nm) than we have seen for coals [4]. This would suggest better connectivity for pores in this size range for the current shale suite compared to coal.

### 3.3. Hg intrusion

Cumulative and incremental intrusion plots using mercury intrusion (Fig. 9a and b) suggest significant pore volume in the meso-macropore range. The Mont 2 sample has the greatest pore

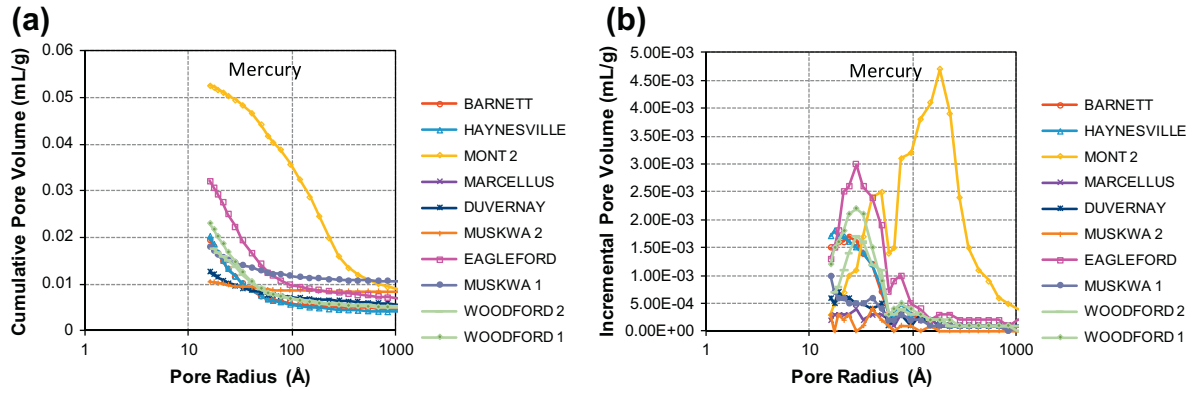


Fig. 9. Cumulative Hg pore volume (a) and incremental pore volume (b) plots for shale sample suite.

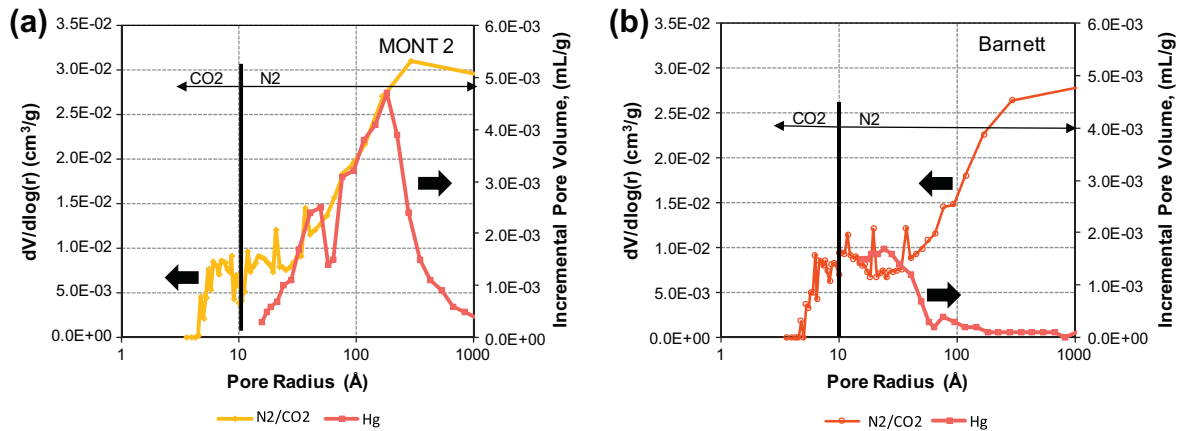


Fig. 10. Comparison of pore size distribution obtained from Hg intrusion (brown curve) and combined CO<sub>2</sub>/N<sub>2</sub> adsorption data for (a) Mont 2 sample and (b) Barnett sample. Small (thin) arrows indicate range of pore sizes covered by N<sub>2</sub> and CO<sub>2</sub> adsorption, and thick arrows indicate the y-axis values corresponding to each curve (Hg intrusion curve is read off of the right axis, N<sub>2</sub>/CO<sub>2</sub> the left axis).

volume, as determined from mercury, while the Duvernay and Muskwa 2 samples have the least. The incremental intrusion plot suggests uni- or multi-modal PSDs for the samples. Most samples have a broad peak between 10 and 100 Å, but the Mont 2 sample shows an additional peak above 100 Å. All samples also have an additional peak at ~350,000 Å (35 μm) (not shown), which may be related to stress–relaxation fracturing of the samples.

As with the carbon dioxide and nitrogen adsorption data, we have attempted to merge the mercury data with the adsorption data (Fig. 10). The Hg data trend is consistent with the adsorption data for pore sizes >30 Å for the Mont 2. For the Barnett sample, the Hg and adsorption data diverge at pore sizes >30 Å. For the other shale samples, agreement between Hg and adsorption is reasonable in some cases, and not for others. There are several possible causes of the discrepancies: Hg intrusion measures pore throats, not bodies, whereas PSDs from desorption (BJH theory) are determined by modeling the progressive removal of adsorbate from pores by multiple processes [25], regardless of whether they represent pore throats or pore bodies. For some pore geometries (ex. slit pores) pore throats are the same as pore bodies – in this case, in theory, adsorption and Hg analysis should yield similar results. It is therefore possible that discrepancies in certain pore size ranges may be due to deviation from a slit-shaped pore geometry. Another possibility, as suggested by Kuila and Prasad [23], is that peak shifting (to smaller pore sizes) can be observed in the Hg data due to the compression of grains at high mercury pressure.

As also suggested by Kuila and Prasad [23], clay samples exhibit multiple scales of porosity [e.g. 26], where pores with diameters between 100 Å and 1000 Å are associated with spaces between clay platelet bundles, pores less than 100 Å are associated inter-layer spaces in the clays, and pores >10,000 Å are associated with pore space between aggregates. Similar observations were made using small-angle scattering techniques [27], including sodium montmorillonite clays (using SAXS and USAXS [28]) as well as

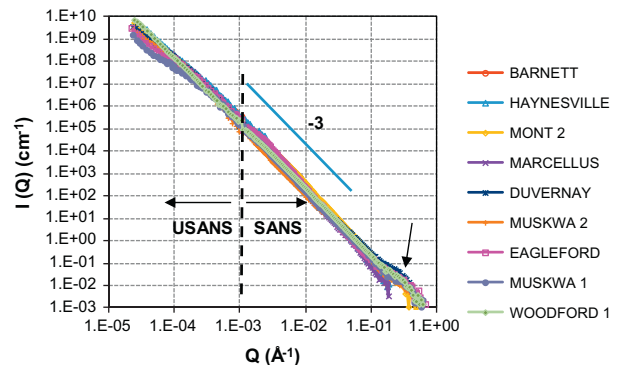


Fig. 11. USANS/SANS patterns subjected to the incoherent background subtraction. Blue line indicates a slope of –3.

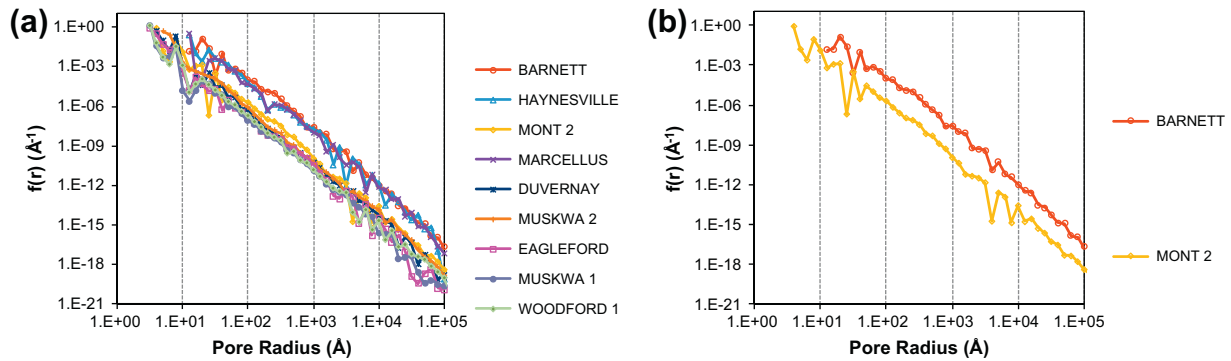


Fig. 12. Pore size distribution function of all shale samples (a) from scattering data. The Barnett and Mont 2 samples are shown in (b).

London clay and Oxford clay using SANS [29]. Mont 2 (Fig. 10a) appears to fit this model quite well, where there is a peak at pore radii  $<10 \text{ \AA}$  (pore diameters  $<20 \text{ \AA}$ ) which could correspond to pore space within clay platelets ( $19 \text{ \AA}$ , [28]) and a peak between 100 and  $1000 \text{ \AA}$  that could be pore space between clay platelet bundles. The third (larger) class of pores appears to be absent, however, possibly owing to sample dewatering. We cannot necessarily make this inference for the other shale samples, however, because the organic matter may also contribute to both micro- and mesoporosity.

### 3.4. SANS/USANS analysis

Fig. 11 shows combined USANS and SANS patterns for all of the shale samples at ambient conditions. In the range of  $10^{-4} < Q < 0.1 \text{ \AA}^{-1}$  the scattering intensity can be represented on the log-log scale by a straight line with a (negative) slope close to  $-3$  (see blue<sup>1</sup> line on Fig. 11), which indicates a power-law scattering characteristic of a very rough (fractal) pore-matrix interface. This  $Q$ -range is dominated by the scattering from pores of linear dimensions in the range  $2.5 \mu\text{m} > 2.5/Q > 25 \text{ \AA}$ . The average slopes for each sample (Table 2) range from  $-3.0$  to  $-3.3$  corresponding to surface fractal dimensions of  $D_s = 3.0$  to  $D_s = 2.7$ , except for Woodford 1 sample (slope =  $-2.9$ ) which is bordering on mass fractal character.

The arrow at  $Q \approx 0.3 \text{ \AA}^{-1}$  ( $2r = 2\pi/Q \approx 21 \text{ \AA}$ ) indicates a “hump” on the scattering curve, which results from a nanometer-scale spatial ordering, possibly related to the interlayer repeat distance of  $19 \text{ \AA}$  (interlayer spacing plus layer thickness, Morvan et al. [28]) in montmorillonite clay minerals. For the Mont 2 sample such an interpretation is very likely, as discussed in the previous section, and it is possible that clay-rich samples also exhibit a similar nanometer-scale ordering. The peak is however rather weak and washed-out, and is superimposed on a falling-off background. Correlation between the clay content based on XRD and the SANS hump intensity is complicated by the fact that SANS detects volume fraction of the layered clays, whereas XRD detects the volume fraction of 3D clay crystals. These two volume fractions may not be identical. In addition, in the high  $Q$  domain coherent SANS scattering ( $I_{coh}$ ) becomes progressively contaminated by incoherent scattering background ( $I_{inc}$ ). As soon as both signals become comparable in the high  $Q$  domain, the hump intensity may become strongly affected by (even small) errors in the determination of  $I_{inc}$ .

Pore size distributions (Fig. 12) were obtained from the fit of the Polydisperse Sphere Particle model using the PRINSAS software [30]. The total pore volume and the SSA (Table 3) were calculated by summing individual pore volumes and their surface areas as a

Table 3  
SANS/USANS calculations.

| Shale sample | SLD<br>( $\times 10^{-6} \text{ \AA}^{-2}$ ) | Exponent | Porosity(%) <sup>a</sup> | Specific surface area ( $\text{cm}^2/\text{cm}^3$ ) <sup>b</sup> |
|--------------|--|----------|--------------------------|--|
| MONT2        | 3.81 <sup>c</sup>                            | -3.2     | 7.88                     | 3.97e5   |
| DUVERENAY    | 4.26   | -3.1     | 6.99                     | 9.56e5   |
| EAGLEFORD    | 4.35   | -3.2     | 6.83                     | 4.59e5   |
| MUSKWA1      | 4.15   | -3.0     | 5.63                     | 4.05e5   |
| MUSKWA2      | 4.28   | -3.1     | 3.95                     | 3.50e5   |
| WOODFORD1    | 4.15   | -2.9     | 7.68                     | 6.17e5   |
| BARNETT      | 4.16   | -3.3     | 5.48                     | 0.98e5   |
| HAYNESVILLE  | 4.29   | -3.3     | 6.18                     | 0.92e5   |
| MARCELLUS    | 4.63   | -3.3     | 3.55                     | 0.34e5   |

<sup>a</sup> Porosity is total porosity.

<sup>b</sup> The probe size for SSA is  $6.31 \text{ \AA}$ ; The probe size for the Barnett and Haynesville samples is  $12.6 \text{ \AA}$ .

<sup>c</sup> The average SLD of Smectite group is calculated based on Montmorillonite. For more accurate SLD, we need to determine the atomic composition of the actual sample using the XRF (X-ray fluorescence) technique.

function of pore radius,  $r$ , and normalizing to the sample volume. We note that there is a high degree of noise in the data for pore radii  $<50 \text{ \AA}$  ( $5 \text{ nm}$ ), which is due to rapidly decreasing scattering intensity at the increased  $Q$ -values.

In order to provide more direct comparison of the SANS/USANS-derived PSDs with those from adsorption data, we have converted pore volume distributions,  $f(r)$ , obtained from SANS/USANS results, into pore volume distributions,  $dV/dr$ , and compared them to the combined  $\text{CO}_2/\text{N}_2$  adsorption data (Fig. 13). Both sets of data were determined on the absolute scale and no scaling factor was used. The agreement between the methods appears to be quite good, despite the difference in (a) sample volume analyzed and (b) in sample preparation. We note that the excessive noise apparent in the SANS/USANS-derived  $dV/dr$  data could be improved in principle, by either significantly increasing the SANS acquisition time or using small-angle X-ray scattering (SAXS) as an alternative method of determining  $f(r)$ .

### 3.5. Determination of accessible versus inaccessible porosity in the Barnett sample

In order to establish the amount of accessible versus inaccessible pores, SANS data were acquired from the Barnett sample saturated with  $\text{CD}_4$ , the “contrast matching fluid”. SANS measurements were performed at several pressures in order to establish the zero average contrast pressure ( $P_{ZAC}$ ). By definition, for a sample with 100% accessible porosity, the intensity of scattering at  $P_{ZAC}$  is nullified because the scattering length density (SLD) of the matrix and fluid in the pore structure are matched. As discussed in the

<sup>1</sup> For interpretation of color in Figs. 1–5, 7–14, 17, the reader is referred to the web version of this article.

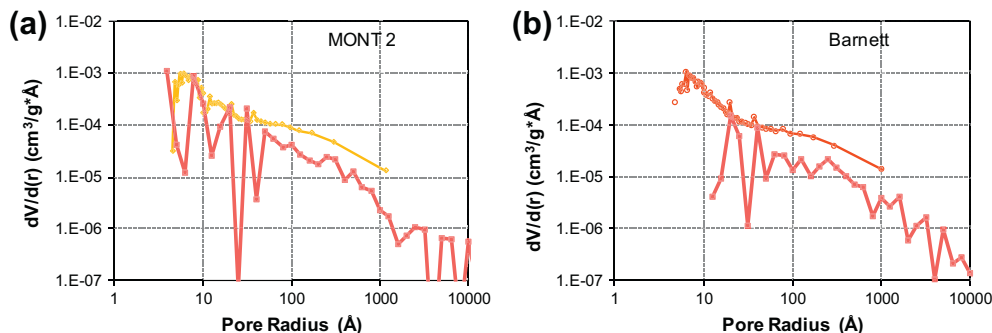


**Fig. 13.** Comparison of pore volume distributions obtained from combined  $\text{CO}_2/\text{N}_2$  adsorption data and SANS/USANS (brown curve) for (a) Mont 2 sample and (b) Barnett sample.

following, in practice  $P_{\text{ZAC}}$  is determined by finding a pressure for which the scattering intensity is at the minimum. For a two-phase (pore/matrix) system, with randomly distributed interconnected pores (ex. shale with pores filled with weakly adsorbing fluid), the SANS intensity,  $I(Q)$ , (neutron cross section per unit volume in units of  $\text{cm}^{-1}$ ) is given by [16]:

$$I(Q) = 4\pi(\rho_s^* - \rho_f^*)^2 c(1 - c)V \int_0^\infty r^2 \gamma_0(r) \frac{\sin(Qr)}{Qr} dr \quad (1)$$

where  $\gamma_0$  is the normal correlation function of the SLD fluctuations;  $(\rho_s^* - \rho_f^*)^2$  is the neutron contrast between the SLD of the solid matrix ( $\rho_s^*$ ) and the SLD of the fluid in the pores ( $\rho_f^*$ , proportional to fluid density);  $c$  is the volume fraction of pores in the sample (total porosity); and  $V$  is the volume of sample illuminated by the neutron beam. It follows from Eq. (1) that the scattering intensity varies linearly with the contrast between the matrix and the fluid in the pores. At low pressures ( $P < P_{\text{ZAC}}$ ),  $\rho_s^* \gg \rho_f^*$  and the intensity decreases as pressure increases. If the pores are accessible to the fluid, at  $P = P_{\text{ZAC}}$ ,  $I(Q)$  approaches zero for every  $Q$ -value since  $\rho_s^* = \rho_f^*$ . As soon as the pressure is further increased above  $P_{\text{ZAC}}$ ,  $I(Q)$  will start increasing again, proportional to the value of  $(\rho_s^* - \rho_f^*)^2$ .

For samples with some inaccessible porosity, residual scattering will be observed, because the fluid trapped in inaccessible pores is

disconnected from the fluid external to the sample, which is confined to the interconnected pore space.

For the Barnett sample, the  $P_{\text{ZAC}}$  was first estimated by measuring USANS intensity versus  $Q$  at multiple pressures of  $\text{CD}_4$ . The intensity measured at each  $Q$  should go through a minimum as the pressure approaches  $P_{\text{ZAC}}$  as illustrated in Fig. 14. The intensity doesn't vary much with pressure above 6039 psi (416.4 bar); this indicates that, to a first approximation,  $I(Q)$  measured at 8000 psi (551.7 bar) should not be no more than  $\sim 5\%$  off that at the zero average contrast (ZAC) condition.

To further illustrate this, Fig. 15 shows the number of neutron counts plotted versus pressure for a single  $Q$ -value within the range of the USANS instrument. The proximity of scattering measured at  $P = 8000$  psi (551.7 bar) to the zero average contrast condition is apparent, as the scattering intensity decreases by a factor of about 2 and reaches a minimum.

Using procedures described in Melnichenko et al. [16], the fraction of porosity accessible to  $\text{CD}_4$  was calculated as a function of  $Q$  (and pore radius,  $2.5/Q$ ), as shown in Fig. 16. The fraction of accessible porosity decreases for pore radii decreasing from 400 Å to 60 Å and is reasonably constant at 0.85 for pore radii in the range from 400 Å to 3000 Å. At pore radii larger than 3000 Å, the fraction of accessible porosity decreases again to around 0.5. This behavior is quite different from that observed in coals by Melnichenko et al. [16], as for one coal sample only (inertinite-rich) did the fraction of accessible porosity decrease at pore radii larger than 1000 Å.

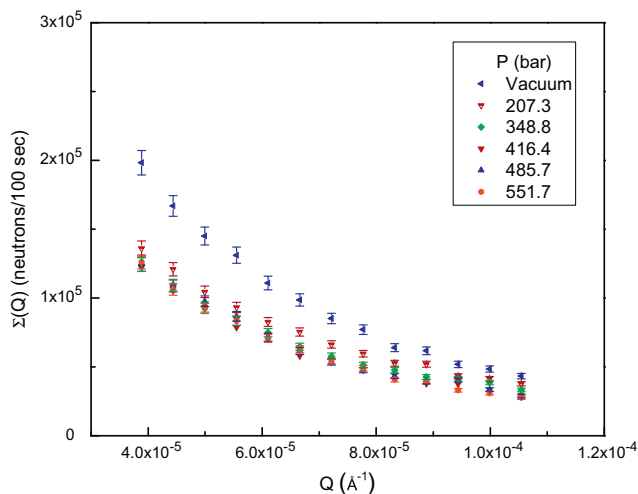


**Fig. 14.** Scattering intensity  $\Sigma(Q)$  (number of neutrons per 100 s) from Barnett shale as a function of  $Q$  in the USANS region  $3.9 \times 10^{-5} < Q < 1.1 \times 10^{-4}$  at different pressures shown in the inset. The intensity at each  $Q$  should go through a minimum as pressure approaches zero average contrast pressure ( $P_{\text{ZAC}}$ ). This figure shows that there is virtually no (within 5%) variation of scattering at pressures higher than 416.4 bar. This indicates that to the first approximation the scattering measured at 8000 psi (551.7 bar) should not be more than  $\sim 5\%$  off that at ZAC.

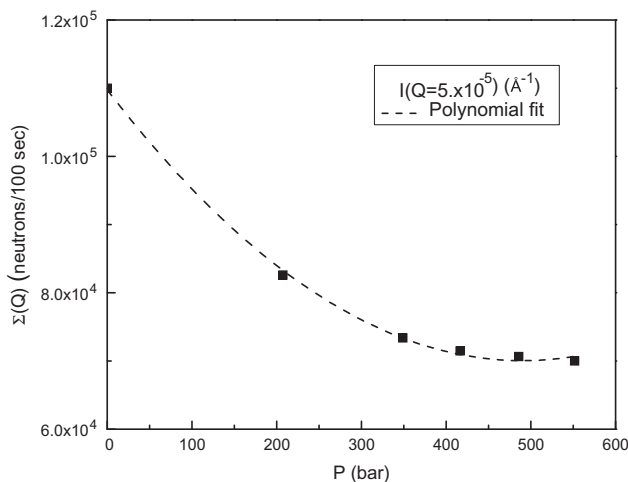


**Fig. 15.** Scattering intensity  $\Sigma(Q)$  (number of neutrons per 100 s) from Barnett shale as a function of pressure at a randomly picked value of  $Q = 5 \times 10^{-5} \text{ \AA}^{-1}$ . Dash line is a polynomial fit with a minimum around 500 bar. It again illustrates proximity of scattering measured at  $P = 8000$  psi (551.7 bar) to zero average contrast condition.

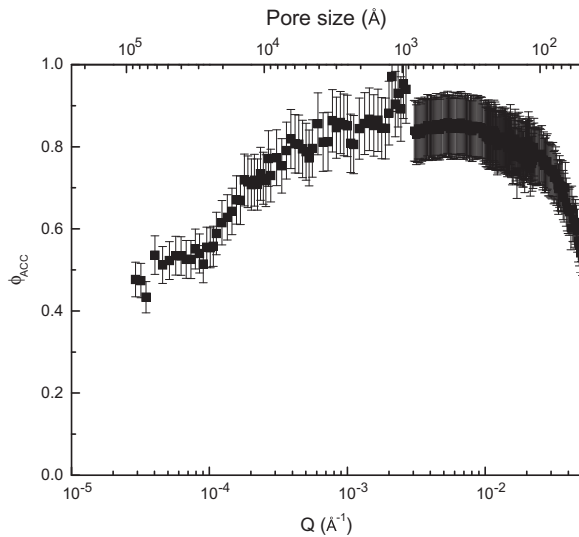


**Fig. 16.** Volume fraction of pores accessible to  $\text{CD}_4$  ( $\phi_{\text{ACC}}$ ) in Barnett shale as a function of the scattering vector  $Q$  and pore size (radius)  $R$ . Error propagation calculations give the total error bars of 8.8% based on assumption that all intensities are known within 5% accuracy and the intensity measured at 551.7 bar is no more than 5% off zero average contrast pressure. Data for  $R < 50 \text{ \AA}$  are not shown as in this region calculated values of  $\phi_{\text{ACC}}$  may be affected by condensation of  $\text{CD}_4$  in small pores.

#### 4. Discussion

The combined use of SANS/USANS with low-pressure adsorption and high-pressure mercury injection is an effective approach for fully characterizing the pore structure of shales. Pore geometry in different size fractions can be inferred from SANS/USANS, as well as the total porosity and fraction of accessible porosity. Scattering plots for shales indicate a power-law scattering characteristic that spans a wide  $Q$ - (and therefore pore size) range. The derived fractal dimensions,  $D_s$ , range from 3.0 to 2.7 and are consistent with a polydisperse sphere model over the pore size (radius) range  $25 \text{ \AA} < 2.5/Q < 2.5 \text{ \mu m}$ . However, for pore radii less than  $25 \text{ \AA}$ , some samples exhibit nanometer-scale spatial ordering, which is likely to be related to interlayer repeat distance (about  $19 \text{ \AA}$ ) in clay minerals. Low-pressure adsorption analysis of the montmorillonite-rich shale sample confirms pore sizes consistent with clay interlayer-spacing.

Combined pore volume distributions from low-pressure ( $\text{CO}_2$  and  $\text{N}_2$ ) adsorption show reasonable agreement with SANS/USANS, despite the fact that SANS/USANS “sees” the entire pore structure whereas adsorption is limited to what is accessible to gas molecules under the conditions of the experiment. For the Barnett sample, the amount of accessible porosity (Fig. 16) is high in the “overlap” region of the SANS/USANS/adsorption analysis ( $100\text{--}1000 \text{ \AA}$ ), which explains the reasonable agreement between pore volume distributions obtained from the two different methods (Fig. 13b). We note in passing that the values of  $\phi_{\text{ACC}}$  presented in Fig. 16 could be used to further re-calibrate the absolute values of SANS-derived  $dV/dr$  (presented in Fig. 13b) with respect to the adsorption-derived  $dV/dr$ . Such a procedure would correct any (small) systematic errors introduced during the SANS/USANS data analysis by using XRD-derived chemical composition of the samples to calculate their scattering length densities (SLDs).

The small fraction of accessible porosity in the large pore size fractions (not quantifiable by sorption) helps explain the low matrix permeability that we see in shales. Clarkson et al. [15], who quantified accessible versus inaccessible porosity by comparing porosity accessible to helium porosimetry and total porosity from SANS/USANS, suggested that permeability may be related to the percentage of accessible porosity. Unfortunately helium porosity

values were not available for this dataset. We speculate that, as observed by Clarkson et al. [15], porosities derived from helium for this shale suite would be smaller than that derived from SANS/USANS because helium allows quantification of accessible porosity only.

The cause of the low-accessibility of larger pores (pore radii  $> 10,000 \text{ \AA}$ ), as determined by the SANS/USANS analysis, is uncertain. There are several possible explanations, including the existence of large isolated vugs in the samples, similar to what is found in some carbonate rocks. It is also possible that some of the larger pores are isolated during re-adsorption of moisture in smaller pore throats. It is further possible that  $\text{CD}_4$  condensation in the smaller (micropores), as noted by Melnichenko et al. (2012) for  $\text{CO}_2$  and methane adsorption in coal, is blocking fluid transport to some of the macropores. The cause of this apparent low accessibility will be investigated in future work.

Although SANS/USANS and low-pressure adsorption measurements gave comparable pore-size distributions, neither technique distinguishes pore bodies from pore throats – this distinction is important for understanding controls on permeability. Mercury porosimetry quantifies pore throat sizes and not pore bodies. Some of the discrepancy noted between incremental intrusion and sorption PSD results may be related to the fact that sorption results provide pore body and throat distributions.

In previous studies of montmorillonite clay samples [23], the pore geometry was interpreted to be slit-shaped, as interpreted from isotherm hysteresis loops. However, the average slope of the SANS/USANS curve obtained from our clay-rich sample (Mont2, Fig. 17) is about  $-3.2$ , indicating polydisperse 3D scattering objects rather than 2D sheets. This discrepancy can only be reconciled if there is some swelling caused by nearly-spherical polydisperse pockets of water confined between the stacks of collapsed nematic phase in the sample. Scattering is then dominated by polydisperse 3D objects, whereas sorption occurs on the walls of multilayer stacks of 2D sheets, practically forming slit pores. Scattering from such a system was modeled by Morvan et al. [28] (also see Fig. 18C in [27]) and their scattering curve is strikingly similar to that presented in Fig. 17 for the Mont2 sample (the modeled curve of Morvan et al. is also reproduced as curve C in Fig. 19 of [29]).

Although it is clear that shale composition (both inorganic and organic) has a control on pore structure of the suite of shale samples, as evidenced by the variability in porosity, pore size distribution and surface area, detailed investigations of composition controls are reserved for future work.

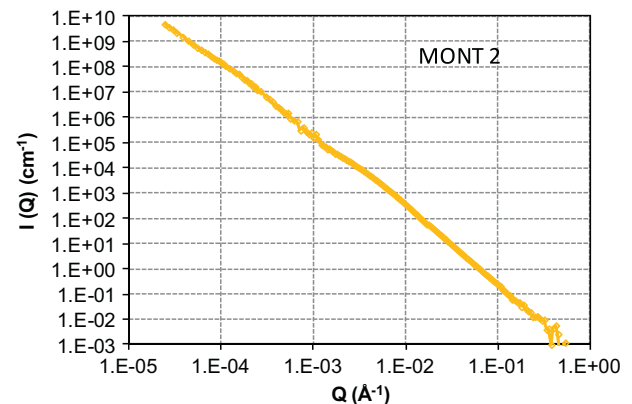


**Fig. 17.** USANS/SANS patterns for Mont 2 sample subjected to background subtraction.

## 5. Conclusion

Low-pressure adsorption, high-pressure mercury intrusion and SANS/USANS analysis of a suite on North American shale gas samples reveal significant differences in pore structure, that in turn will affect both gas storage and transport properties. The following can be concluded about the pore structure of these samples:

- (1) Strong differences in BET surface area, nitrogen- and carbon dioxide-derived pore volumes exist between samples
- (2) Pore size distributions obtained from N<sub>2</sub> and CO<sub>2</sub> adsorption analysis can be effectively combined to reveal information about micro–meso–macroporosity up to a limit of ~1000 Å
- (3) Pore size distributions from adsorption analysis may be uni- or multi-modal.
- (4) Incremental mercury intrusion yields information about pore throats only, which in part explains discrepancies with adsorption-derived results.
- (5) SANS/USANS scattering plots suggest power-law scattering indicating a wide-range of pore radii. A “hump” appears at high *Q*-values (small pore sizes) for some samples, indicating nanometer-scale spatial ordering, possibly related to inter-layer spacing in clay minerals.
- (6) SANS/USANS-derived pore volume distributions are in reasonable agreement with low-pressure adsorption.
- (7) Accessible porosity estimates were successfully obtained for a Barnett shale sample and suggested that accessible porosity is pore-size-dependent.

## Acknowledgements

Chris Clarkson would like to acknowledge Encana for support of his Chair position in Unconventional Gas at the University of Calgary. Funding for Nisael Solano's work was provided in part by a Society of Petroleum Engineers Canada Region STAR Fellowship provided to Solano as well as by the sponsors of the Tight Oil Consortium, hosted at the University of Calgary.

Marc Bustin would like to acknowledge Geoscience BC for a grant provided to support this research.

The authors would also like to acknowledge D.F.R. Mildner for his help during USANS experiments. The research at Oak Ridge National Laboratory's High Flux Isotope Reactor was sponsored by the Laboratory Directed Research and Development Program and the Scientific User Facilities Division, Office of Basic Energy Sciences, US Department of Energy. This research was supported in part by the ORNL Postdoctoral Research Associates Program, administered jointly by the ORNL and the Oak Ridge Institute for Science and Education. The elements of this work utilizing the BT-5 instrument at the NCNR were supported in part by the National Science Foundation under agreement No. DMR-0454672.

## References

- [1] Bustin RM, Bustin AMM, Cui X, Ross DJK, Murthy Pathi VS. Impact of shale properties on pore structure and storage characteristics. In: SPE paper 119892 presented at the society of petroleum engineers shale gas production conference in Fort Worth, Texas; November 16–18, 2008.
- [2] Clarkson CR, Jensen JL, Blasingame TA. Reservoir engineering for unconventional gas reservoirs: what do we have to consider? In: SPE paper 145080 presented at the society of petroleum engineers North American unconventional gas conference and exhibition, Woodlands, Texas; June 12–16, 2011.
- [3] Gan H, Nandi SP, Walker Jr PL. Nature of the porosity in American coals. *Fuel* 1972;51:272–7.
- [4] Clarkson CR, Bustin RM. The effect of pore structure and gas pressure upon the transport properties of coal: a laboratory and modeling study. 1. Isotherms and pore volume distributions. *Fuel* 1999;78:1333–44.
- [5] Mastalerz M, Drobnik A, Strąpoć D, Solano Acosta W, Rupp J. Variations in pore characteristics in high volatile bituminous coals: implications for coalbed gas content. *Int J Coal Geol* 2008;76:205–16.
- [6] Lahann R, Mastalerz M, Rupp JA, Drobnik A. Influence of CO<sub>2</sub> on New Albany Shale composition and pore structure. *Int J Coal Geol*, in press. doi: <http://dx.doi.org/10.1016/j.coal.2011.05.004>.
- [7] Chalmers GRL, Bustin RM. The organic matter distribution and methane capacity of the Lower Cretaceous strata of Northeastern British Columbia. *Can Int J Coal Geol* 2007;70(1–3):223–39.
- [8] Strąpoć D, Mastalerz M, Schimmelmann A, Drobnik A, Hasenmueller NR. Geochemical constraints on the origin and volume of gas of the New Albany Shale (Devonian – Mississippian) in the eastern part of the Illinois Basin. *AAPG Bull* 2010;94:1713–40.
- [9] Ross DJK, Bustin RM. The importance of shale composition and pore structure upon gas storage potential of shale gas reservoirs. *Mar Petrol Geol* 2009;26(6):916–27.
- [10] Radlinski AP, Mastalerz M, Hinde AL, Hainbuchner M, Rauch H, Baron M, et al. Application of SAXS and SANS in evaluation of porosity, pore size distribution and surface area of coal. *Int J Coal Geol* 2004;59:245–71.
- [11] Melnichenko YB, Radlinski AP, Mastalerz M, Cheng G, Rupp J. Characterization of the CO<sub>2</sub> fluid adsorption in coal as a function of pressure using neutron scattering techniques (SANS and USANS). *Int J Coal Geol* 2009;77:69–79.
- [12] Sakurovs R, Radlinski AP, Melnichenko YB, Blach T, Cheng G, Hartmut L, et al. Stability of the bituminous coal microstructure upon exposure to high pressures of helium. *Energy Fuels* 2009;23:5022–6.
- [13] Mares TE, Radlinski AP, Moore TA, Cookson D, Thiagarajan P, Ilavsky J, et al. Assessing the potential for CO<sub>2</sub> adsorption in a subbituminous coal, Huntley Coalfield, New Zealand, using small angle scattering techniques. *Int J Coal Geol* 2009;77:54–68.
- [14] Gethner JS. The determination of the void structure of macroporous coals by small-angle neutron scattering: void geometry and structure in Illinois No-6 bituminous coal. *J Appl Phys* 1986;59:1068–85.
- [15] Clarkson CR, Freeman M, He L, Agamalian M, Melnichenko YB, Mastalerz M, et al. Characterization of tight gas reservoir pore structure using USANS/SANS and gas adsorption analysis. *Fuel* 2012;95:371–85.
- [16] Melnichenko YB, He L, Sakurovs R, Kholodenko AL, Blach T, Mastalerz M, et al. Accessibility of pores in coal to methane and carbon dioxide. *Fuel* 2012;91:200–8.
- [17] <http://www.nist.gov/data/nist23.htm>.
- [18] Barker JG, Glinka CJ, Moyer JJ, Kim MH, Drews AG, Agamalian M. Design and performance of a thermal-neutron double-crystal diffractometer for USANS at NIST. *J Appl Crystallogr* 2005;38(6):1004–11.
- [19] Radlinski AP, Boreham CJ, Lindner P, Randl OG, Wignall GD, Hinde A, et al. Small angle neutron scattering signature of oil generation in artificially and naturally matured hydrocarbon source rocks. *Org Geochem* 2000;31:1–14.
- [20] Chathoth SM, Mamontov E, Melnichenko YB, Zamponi M. Diffusion and adsorption of methane confined in nano-porous carbon aerogel: a combined quasi-elastic and small-angle neutron scattering study. *Microporous Mesoporous Matter* 2010;132:148–53.
- [21] Gregg SJ, Sing KSW. Adsorption, surface area, and porosity. 2nd ed. New York: Academic Press; 1982.
- [22] Rietveld HM. Line profiles of neutron powder-diffraction peaks for structure refinement. *Acta Cryst* 1967;22:151–2.
- [23] Kuila U, Prasad M. Surface area and pore-size distribution in clays and shales. In: SPE paper 146869 presented at the society of petroleum engineers annual technical conference and exhibition, Denver, Colorado; October 30–November 2, 2011.
- [24] Brunauer S, Deming LS, Deming WS, Teller E. On a theory of the van der Waals adsorption of gases. *J Am Chem Soc* 1940;62:1723–32.
- [25] Adesida AG, Akkutlu IY, Resasco DE, Rai CS. Kerogen pore size distribution of Barnett Shale using DFT analysis and monte carlo simulations. In: SPE paper 147397 presented at the society of petroleum engineers annual technical conference and exhibition, Denver, Colorado; October 30–November 2, 2011.
- [26] Aylmore LAG, Quiek JR. The micropore size distribution of clay mineral systems. *J Soil Sci* 1967;18:1–17.
- [27] Radlinski AP. Small-angle neutron scattering and the microstructure of rocks. *Rev Mineral Geochem* 2006;63:363–97.
- [28] Morvan M, Espinat D, Lambard J, Zemb T. Ultrasmall- and small-angle X-ray scattering of smectite clay suspensions. *Colloids Surf A* 1994;82:193–203.
- [29] Allen AJ. Time-resolved phenomena in cements, clays and porous rocks. *J Appl Crystallogr* 1991;24:624–34.
- [30] Hinde AL. PRINSAS – a windows-based computer program for processing and interpretation of small-angle scattering data tailored to the analysis of sedimentary rocks. *J Appl Crystallogr* 2004;37:1020–4.